Chemical Engineering Journal 464 (2023) 142635

Contents lists available at ScienceDirect

Chemical Engineering Journal

journal homepage: www.elsevier.com/locate/cej

Solvent engineering for triple cationic ITO-based mesoscopic tin perovskite solar cells

Donghoon Song [a], Hung-Yu Tseng [a], Sudhakar Narra [a,b], I-Hua Tsai [a], Eric Wei-Guang Diau [a,b,*]

[a] Department of Applied Chemistry and Institute of Molecular Science, National Yang Ming Chiao Tung University, 1001 Ta-Hsueh Rd., Hsinchu 30010, Taiwan
[b] Center for Emergent Functional Matter Science, National Yang Ming Chiao Tung University, 1001 Ta-Hsueh Rd., Hsinchu 30010, Taiwan

ARTICLE INFO

Keywords:
Lead-free tin perovskites
Dimethylpropyleneurea
Solvent engineering
Cation engineering
Mesoscopic solar cells

ABSTRACT

Besides negligible toxicity, tin-based perovskite solar cells (TPSCs) hold bright prospects in light of broad light harvesting beyond ~850 nm rendering theoretical efficiencies higher than lead-based counterparts. However, tin perovskites which are as thin as ~200 nm (cf., ~500 nm or beyond for lead analogs) and populate tin defects (i.e., Sn^{4+} defects) especially on a top surface do not suffice to absorb all the incoming light and to convert it into electricity. Herein, we explore triple mesoscopic TPSCs and develop suitable tin perovskites via cation and solvent engineering. The predetermined body frame of TiO_2 (ETM) / Al_2O_3 (insulator) / ITO (HTM and electrode) mesoporous scaffolds enables thickness control of tin perovskites with ease over micrometers (~2 μm herein), where ETM stands for the electron transport material and HTM stands for the hole transport material. In mesoscopic TPSCs, ITO is partly buried in tin perovskites so that the Sn^{4+} defects-enriched surface is least influential to charge transfer. By leveraging a Cs cation and a *N*,*N*′-dimethylpropyleneurea solvent, demanding quality of tin perovskites for efficient conversion of light-to-electricity is satisfied such as relaxed and passivated crystals and Sn^{4+}-lean defects. The resulting perovskites are well-suited in performance and stability to the mesoscopic TPSCs. Importantly, they are highly reproducible and attain high quantum efficiency of >90% over a broad range of light absorption from 400 to 700 nm. This remarkable quantum efficiency translates to photocurrent higher than >27 mA cm^{-2} (cf., theoretical limit: ~31 mA cm^{-2}). We herein enlighten the future of TPSCs by proposing a route for maximal light harvesting and its conversion.

1. Introduction

Fossil fuels impose irreparable damage to the globe and must be replaced by green energy sources in the near future. Renewable energy is an attractive option to replace fossil fuels, epitomized by solar cells (SCs). The key to SC operation is to maximize the conversion of solar energy to electricity in a broad light absorption range, now silicon (Si)-based SC is the mainstream for solar energy conversion. However, Si SC is cost-intensive for its fabrication using high purify silicon wafers. Perovskite solar cells (PSCs) play a game changer in the photovoltaic league with the advantages of solution-processability (i.e., cost-efficiency), lightweight, and mechanical flexibility with high efficiency of over 25%, which is comparable to its c-Si analogue [1,2]. PSCs can reach photocurrent >25 mA cm^{-2} as a result of high conversion of light to electricity (typically, >80%) within a bandgap of ~1.5 eV. However, the toxic element of lead (Pb) in the perovskites stands in the way to hinder the commercial deployment of PSCs.

While there exist two routes of sequestration or replacement of lead, seeking the latter with elements such as tin, copper, antimony, germanium, etc. can be a more reliable, efficient, and environmental choice. Beyond resolving the toxicity issue, the high charge carrier mobility, slow carrier relaxation, and importantly, ideal bandgap (~1.2–1.4 eV) – smaller than that for lead counterparts (cf., ~1.5 eV for formamidinium lead triiodide, $FAPbI_3$) and on the other hand close to the Shockley-Queisser limit – make tin (Sn)-based PSCs (TPSCs) glittering most among the replacements [3]. Progressing fundamental technologies of tin perovskites can propel not only solar cells but also diverse applications including light-emitting diodes [4], photodetectors [5], transistors [6], lasers [7], photocatalysts [8] and X-ray imaging [9].

Unlike lead PSCs, p-i-n architectures (e.g., ITO / PEDOT:PSS / tin perovskite / C60 / BCP / Ag) prevail for high-performance TPSCs, where ITO is the indium tin oxide-coated glass substrate, PEDOT:PSS is the poly

* Corresponding author at: Department of Applied Chemistry and Institute of Molecular Science, National Yang Ming Chiao Tung University, 1001 Ta-Hsueh Rd., Hsinchu 30010, Taiwan.
E-mail address: diau@nycu.edu.tw (E. Wei-Guang Diau).

https://doi.org/10.1016/j.cej.2023.142635
Received 31 December 2022; Received in revised form 22 March 2023; Accepted 24 March 2023
Available online 25 March 2023

(3,4-ethylenedioxythiophene)-poly(styrenesulfonate), C60 is the fullerene, BCP is the bathocuproine, and Ag is the silver [10]. Mostly, tin perovskite layers were deposited by a spin-coating method. The research advances in the TPSCs lie in the exploration of mixed cations (e.g., GA^+/FA^+ and Cs^+/FA^+) where GA^+ represents the guanidinium cation, and Cs^+ represents the cesium cation [11–17], mixed (pseudo)halides [18–22], additives (e.g., SnF_2 and $EDAI_2$) where SnF_2 represents the tin (II) fluoride, and $EDAI_2$ represents the ethylenediammonium diiodide [23–30], alloying,[31], solvent engineering (e.g., DEF and DMPU) where DEF stands for the diethylformamide, and DMPU stands for the *N*, *N*′-dimethylpropyleneurea [32–34], and many others [35–38], targeting for suppressing oxidation of Sn^{2+} to Sn^{4+}, interfacial passivation, and/or crystal regulation. Especially, embedding Cs cations can significantly strengthen the lifetime of tin perovskites [17]. Interestingly, the additive $EDAI_2$ leads to the opening of bandgap at a large amount (~10% or more) on account of the formation of 3D hollow perovskite crystals [39]. Post-treatment is implemented towards repairing Sn^{4+} defects that are densely populated atop perovskites [40]. With less attention but bright prospects, reports on interface materials (e.g., ICBA ETMs, SAMs) where ICBA stands for the indene-C60 bisadduct, ETM stands for electron transport material, and SAM stands for self-assembled monolayer [41,42], and scalable methods (e.g., two-step deposition)[43,44] have already been reported. However, the p-i-n TPSCs sustain quantum efficiency lower than 80%, which is especially depressed to a great extent at a longer wavelength (e.g., from ~650 nm to the absorption onset).

Sufficient thickness of perovskite, within effective diffusion length of charge carriers, ensures complete harvesting of incoming lights and their conversion to electricity. The state-of-the-art lead perovskites attain film thickness>500 nm via spin coating [1], and their single crystals can reach ~20 μm thickness (cf., ≥100 μm for c-Si SCs) [45]. In contrast, tin perovskites are bound in thickness to ~200 nm or less in spite of possessing larger charge carrier mobilities and similar absorption coefficients compared to their lead counterparts [46]. The hole doping by Sn^{4+} defects can further weaken the absorption ability in longer wavelengths and the charge transfer [46]. The carrier diffusion length of tin perovskites can reach the micrometer scale [47]. The simplest strategy for thicker films prepared by spin-coating needs concentrated precursor solutions and hence leaves more solid contents on substrates following annealing. Tin perovskites are a crystalline material whose film quality (e.g., crystallinity, roughness, pinhole defects, etc.) dominates the device performance. However, the rapid crystallization, greater than lead counterparts [48], upon antisolvent dripping greatly challenges the formation of thick tin perovskites of demanding quality at a high precursor concentration >1 M of tin(II) iodide (SnI_2) [18]. We emphasize that this crystallization is subtle being highly impacted by residual antisolvents and antisolvent injection (delivery time: less than ±~1 s) techniques [42]. Spin-coating may not be a good option for tin perovskites, which can promote tin oxidation on a top surface by an orthogonal flow of ambient air. In this regard, establishing thick films of tin perovskites of demanding quality with film thickness >500 nm to attain high quantum efficiency (>80%) remains an urgent task to surmount in the research community of TPSCs.

Mesoscopic PSCs take both advantages of PSCs and scalability [22,49,50]. In light of up-scaling production, they are a propitious candidate due to being all-solution-processable (even for a top electrode) and additive like printing newspapers. They are comprised of FTO substrate / TiO_2 compact layer (CL) / mesoporous scaffolds of TiO_2 (ETM) / Al_2O_3 (insulating layer) / carbon (electrode and hole transport material, HTM) where tin perovskite is deposited, following infiltration and annealing of its solution droplet, into the TiO_2 and Al_2O_3 and bury carbon to a little extent. Tin perovskite can grow in the scaffolds with continuity with ease. Moreover, it does not use antisolvents and hence crystallizes slowly in relation to solvent evaporation rate to enable thick films of demanding quality. This can permit excellent compatibility with a myriad set of tin perovskites. Besides, distinct from the p-i-n (or n-i-p) PSCs, the top surface of perovskites is not in contact with HTM (or ETM).

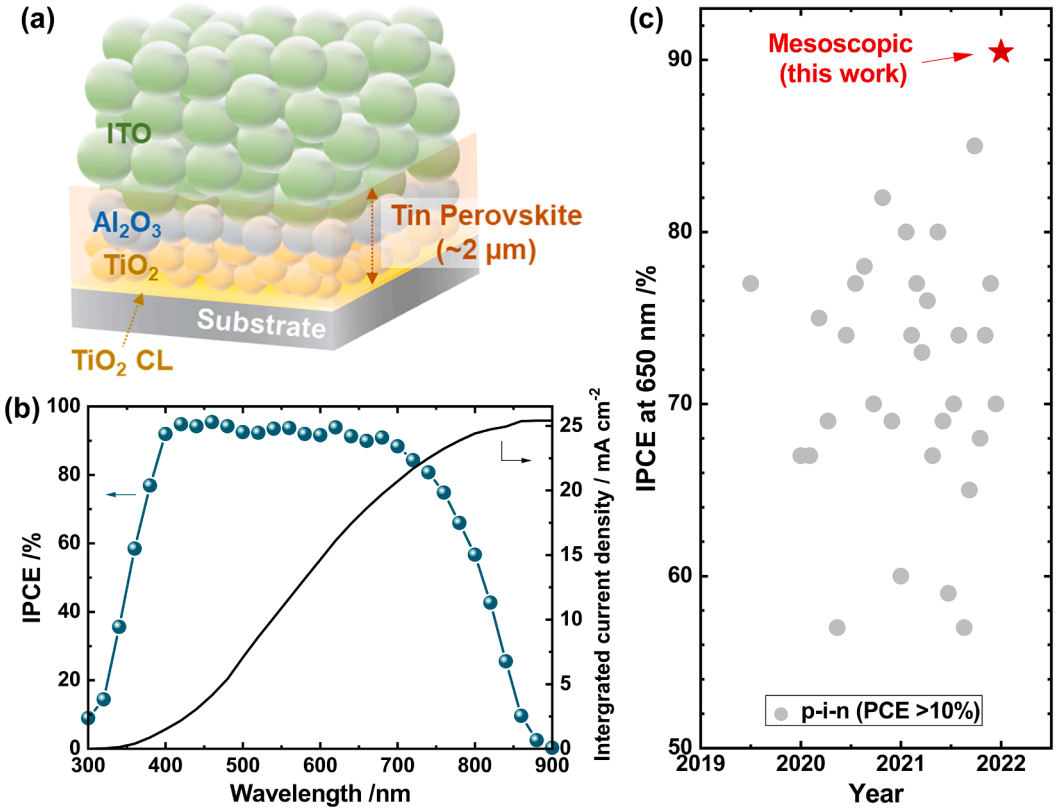

Fig. 1. (a) Illustration and (b) IPCE spectra of mesoporous TPSCs incorporating thick tin perovskite. (c) IPCE values at a wavelength of 650 nm collected from high-performance (>10%) TPSCs.

The mesoporous TPSCs are thus not liable to surface defects-driven deterioration of charge kinetics. Perovskite thickness is readily controllable at a micrometer level by adjusting the thickness of the TiO_2 and Al_2O_3 layers [22,49,50], advantageous for the formation of thick films. The principal task is to completely infiltrate and anneal the precursor solution into the scaffold layers.

According to our precedented research, for superior light-to-electricity conversion, mesoscopic PSCs can be upgraded by replacing carbon with light-reflective ITO nanoparticles (Fig. 1a) [49]. Moreover, the adverse process of interface recombination can be suppressed for concurrent rises in photovoltage and photocurrent and hence a promoted efficiency rise [49]. It was confirmed that the mesoscopic ITO PSCs are greatly compatible with tin perovskites which possess a large bandgap (1.61 eV). The major reason for such bandgap originates from the use of $EDAI_2$ at a large amount (15%), which is needed for interface passivation. However, the strain of the perovskite lattice concurrent with the bandgap was adversely elevated. In this research, by judicious engineering of major components such as cations and solvents, we obtained tin perovskites with a suitable bandgap of 1.44 eV and relaxed crystal lattices even though the same amount of $EDAI_2$ was incorporated. The small bandgap is owing to the formation of a heterojunction structure of 3D perovskite (in bulk) and 3D hollow perovskite (close to ITO). This was enabled by the use of cosolvents of distinct volatilities and by selective coordination of a less volatile solvent with $EDAI_2$. So, upon annealing quick evaporation of the volatile solvent proceeds to form 3D perovskite in bulk and to push the less volatile solvent to the surface where $EDAI_2$ is localized to a large extent for 3D hollow perovskite. This is different from common cation and solvent engineering taking effect over the entire cross-sections of perovskite films, and is simpler than typical heterojunction approaches needing the two-step sequential deposition. Meanwhile, the small bandgap perovskites are completely infiltrated into the scaffolds with continuity. Importantly, they are endowed with demanding film properties of tin perovskites for micrometer-thickness (~2 μm), including reduced microstrain, passivated interface, and lean Sn^{4+} defects. In the mesoscopic TPSCs, they render broad intense quantum efficiency of ~90% over a range of 400–700 nm while retaining >50% at 800 nm. As a result, the TPSCs attain the unprecedently high efficiency of 90.5% at 650 nm, concomitant with photocurrent higher than >27 mA cm^{-2}, approaching the theoretical limit (~31 mA cm^{-2} for the bandgap). Moreover, they are endowed with promising operational stability, exemplified by continual steady output (with merely a 10% drop) under maximum power point light soaking for 6500 s and merely 5% degradation during shelf storage for 1000 h.

2. Results and discussion

The Shockley-Queisser limit, an indicator for maximum theoretical efficiency of SCs, conveys that short circuit current (J_{SC}) as high as ~29–40 mA cm^{-2} is attainable at a perovskite bandgap of 1.2–1.5 eV. The frequently reported J_{SC} for $FASnI_3$ (~1.4 eV) is below 25 mA cm^{-2}, which is still far behind the theoretical J_{SC} by ~10 mA cm^{-2} [3,10,46,51–53]. J_{SC} can be analyzed by incident photon to current conversion efficiency (IPCE) at a wavelength of ~300–1000 nm. It is identified from most literature that high-performance p-i-n TPSCs face two issues: depressed IPCE at a longer wavelength (≥650 nm) and overall low IPCE (<80%) [10].

IPCE is governed by how efficiently incoming lights and attendant charge carriers are collected through perovskite, ETM, HTM, electrodes, and contacts thereof. It is worthwhile noting that due to the exciton binding energy of 3D tin perovskites smaller than thermal energy at room temperature, the generated carriers are free charges. The high IPCE perovskite films need to be sufficiently thick for complete harvesting of lights and to be defects-lean for subsequent generation and collection of abundant free charge carriers. However, tin perovskites are too thin. Furthermore, the abundant Sn^{4+} defects aggravate the effect of charge recombination. For example, they incur the Burstein-Moss effect by which the practical bandgap of perovskites increases. In addition, Sn^{4+} defects populated on the surface would be detrimental to the overall collection of the charge carriers. In particular, interface recombination could be accelerated in relation to decreasing perovskite thickness [54]. In the end, inferior IPCE, including a greatly weakened response at a long wavelength near absorption onset, is yielded. Here the reported films of tin perovskites that are ~2 μm thick and Sn^{4+} defects-lean outperform the thin films to enable excellent IPCE of ≥80% over a broad light absorption range (400–780 nm) as Fig. 1b exhibits where the spectral onset is ~860 nm. Importantly, Fig. 1c compares IPCE at a wavelength of 650 nm, obtained from recent literature where our TPSC attains the highest value of 90.5%. Each data point is summarized in Table S1. The deficit in J_{SC}, calculated by (ideal J_{SC}) – (J_{SC} from IPCE), falls in a smaller value of ~5 mA cm^{-2} than that (>10 mA cm^{-2}) for thin films. We elaborate on the principal approaches and attendant results and discussion for such attainment in the following sections.

In our preceding work [49], tin perovskites of $GA_{0.2}FA_{0.8}SnI_3$ with 15% $EDAI_2$ and 20% SnF_2 were used in the mesoscopic TPSCs. The GA^+ is a co-cation with a zero electric-dipolar moment and the SnF_2 is an additive, both of which are helpful in suppressing tin oxidation for better stability. The addition of a small amount (~1%) of $EDAI_2$, adopted in high-performance p-i-n TPSCs, establishes it as a multifunctional additive for passivating interfacial defects (for charge collection), stitching grain boundaries (for continuity of crystals) and discouraging tin oxidation (for stability) [11,26]. In the mesoscopic TPSCs, according to the large interface areas of contact materials a large amount (15%) of $EDAI_2$ is required for passivation as evident in Figure S1 and Table S2. However, it leads to 3D hollow tin perovskite whose bandgap is augmented by 0.1–0.2 eV at the 10–20% addition [39,49]. Even though EDA^{2+} is too large in size (375 pm of the distance between two ammonium groups in $H_3NCH_2CH_2NH_3^{2+}$) according to the Goldschmidt rule, it can go into 3D perovskite crystal lattices by hollowing out tin iodide fragments but do not discontinue 3D structures [39]. Relevant illustrations are depicted in Fig. 2a. We note that EDA^{2+} deviates from other bulky cations like BA^+ or PEA^+, where BA^+ represents the butylammonium cation, and PEA^+ represents phenylethylammonium cation, inducing low dimensional structures. Meanwhile, the 3D hollow perovskites are subjected to the weakened overlap of tin and iodide orbitals, and hence the narrower bandwidths and wider bandgap. On the other hand, the 3D hollow perovskites are subjected to lattice expansion of elevating strain in the crystal lattices [11,39].

In order to upgrade the old version of tin perovskite, two approaches of cation and solvent engineering are developed. Since Cs^+ (167 pm) is an inorganic cation that is smaller in ionic radius than organic cations such as FA^+ (253 pm) and GA^+ (278 pm), its incorporation can improve stability and performance, for example, by shortening the bandgap and relaxing the lattice crystal as schematic demonstration shown in Fig. 2a. Regardless of optoelectrical properties, the infiltration of perovskites is fundamental in mesoscopic TPSCs while formation of perovskites having a top surface being smooth and defect-lean is pivotal in p-i-n TPSCs. This highlights the necessity of formation of excellent interfaces of perovskites, and hence, no matter what types of perovskites and devices are explored, testing the performance of components at a device level is required. We have thus performed preliminary tests on the mesoscopic TPSCs by embedding Cs^+ into tin perovskites with three distinctive and wide compositions: $Cs_xFA_{1-x}SnI_3$ (x = 0.10–0.65), $Cs_xGA_{0.2}FA_{0.8-x}SnI_3$ (x = 0.05–0.50), and $Cs_xGA_{0.2-x}FA_{0.8}SnI_3$ (x = 0.025–0.2) in the presence of the $EDAI_2$ and SnF_2. The corresponding photovoltaic performances are summarized in Figure S2 and Table S3-S5. Overall, an incremental Cs^+ amount to over ~20% that significantly limits wetting of the solutions was detrimental to infiltration of tin perovskites into the mesoporous scaffolds and hence generation of photocurrent in devices. The most inspiring results came from $Cs_xGA_{0.2-x}FA_{0.8}SnI_3$ (where x (%) = 0, 2.5, 5, 10, 15, 20) in which the perovskite solutions were formulated by dissolving 1 M SnI_2, 0.8 M FAI, 0–0.2 M CsI, 0–0.2 M GAI, 0.15

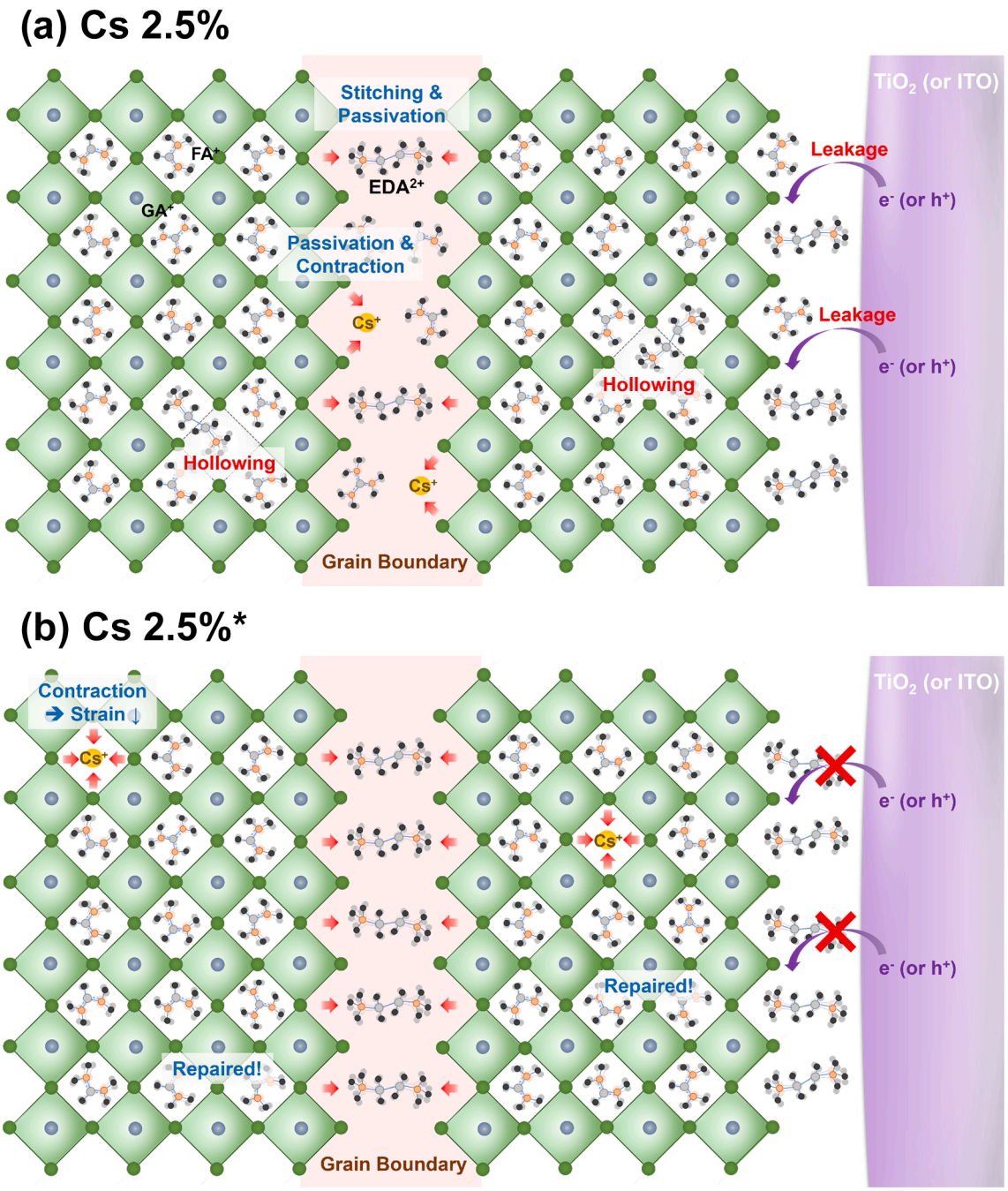

Fig. 2. Schematic demonstration showing the major cation effects of crystals of tin perovskites of (a) Cs2.5 and (b) Cs2.5* in bulk and on interfaces of TiO_2 and ITO. In short, Cs^+ leads to lattice contraction in bulk while EDA^{2+} hollows out the sn-I octahedron. Especially, EDA^{2+} is proficient to stitch the two adjacent crystals via hydrogen bond of NH^{3+}s with I^-s in sn-I octahedra and suppress leakage of electrons (or holes) at the interfaces. For simplicity, SnF_2 was not drawn.

M $EDAI_2$, 0.2 M SnF_2 in cosolvents. They are hereafter coded as Cs 0%, 2.5%, 2.5%*, 5%, 10%, 15%, and 20% where an asterisk represents a dissimilar cosolvent system. All of the cosolvents are miscible as presented in Figure S3. We explore this composition for a systematic study.

The cosolvents except for Cs 2.5%* are comprised of dimethylformamide (DMF) and dimethylsulfoxide (DMSO) at an equal volume ratio. Both DMF and DMSO are used as solvents for crystallization. DMF is essential to promote infiltration of the perovskite solution in the mesoporous scaffolds. DMSO is less volatile and upon removal of DMF at an initial stage of annealing slows down the rapid perovskite crystallization by its strong coordination with SnI_2. For Cs 2.5%*, DMSO is replaced by DMPU at the same composition except for the reduced SnF_2 amount (15%) due to the solubility and the reduced solvent ratio (2:8, v/v) due to the limited wetting-driven performance (Fig. S4a and Table S6). Relative to DMSO, the higher donor number along with lower volatility of DMPU can retard not only the rapid crystallization but also serve as a stable solvent unlike DMSO catalyzing the tin oxidation [33]. Most importantly, DMPU coordinates strongly and selectively with EDA^{2+} as the FTIR spectra in Figure S3 exhibit.

The prepared solutions were yellowish and dropped atop the mesoporous scaffolds. The solution volume was set to 5 μL per active area (cm^2) for an optimal loading amount of tin perovskite. In particular, the surplus amount led to a pile-up of tin perovskite for enhanced charge recombination. The solutions were heated at 70 °C prior to dropping likely to decline their surface tension to facilitate infiltration. Annealing was performed via a two-step temperature procedure, 70 °C for ~3 min

for complete infiltration of the solution into the mesoporous scaffolds and 100 °C for 15 min for perovskite crystallization. In particular, it was capped with a glass vial during the first step, after which the DMSO/DMF film stayed in yellow color whereas the DMPU/DMF film was turned from yellow to dark grey as a result of rapid removal of dominant DMF. Relative to DMSO and DMPU, DMF is pretty volatile possessing the low boiling point and high vapor pressure [55]. DMSO was evaporated within ~1 min. DMPU was slowly evaporated over the time course of ~5 min to result in a complete change in color from dark grey to dark black. The removal of solvents upon annealing is evidenced by the FTIR spectra in Figure S5. The photos displayed in Figures S6a and b show this color change clearly. Micrometer-thick (~2 μm herein) films of tin perovskites in the mesopores were then produced; we note that the perovskite content is considerably smaller than that for the p-i-n PSCs because of the significant contents of TiO_2 and Al_2O_3. Photographs were thereafter taken from both sides: the bottom (substrate) and top (ITO) sides, as shown in Fig. 3a. In common, the small bandgap perovskites being black in color in the mesoporous scaffolds are observed from the bottom, an indication of excellent perovskite infiltration and crystallization. This crystallization is distinct from thin tin perovskites prepared by the antisolvent method which likely triggers crystallization from the surface [56]. On the other hand, it may be advantageous over formation of thick films of tin perovskites. Because perovskites are mostly deposited into the TiO_2 and Al_2O_3 layers, and a lower region (close to Al_2O_3) of ITO, perovskites appear grey in color from the top. However, there exists one exception for Cs 2.5%* which is tinged with orange color while the TiO_2 side is black for all. While $EDAI_2$ is white itself, this distinct color formation imparts formation of a heterojunction film. By acquiring spectra of X-ray photoelectron spectroscopy (XPS) the heterojunction is identified, as shown in Figure S7. Heterojunction structures (e.g., 3D/2D perovskites) are usually fabricated using two deposition steps, however, our heterojunction necessitates only a single deposition step, which could expand the design and process space of perovskite structures. Meanwhile, we note that it did not emerge for Cs 2.5% at the same cosolvent ratio (DMSO:DMF = 2:8, v/v) for Cs 2.5%*. The origin of the heterojunction likely arises from DMPU. This is crystallized as DMF was replaced by DEF performing a similar role as DMF but having less volatility, the results of which are presented in Fig. S4b and Table S7 and confirm the same DMPU effects. On the other hand, the results add flexibility in designing cosolvents.

By measuring spectra of light absorption (Fig. 3b) and photoluminescence (PL) (Fig. 3c), we scrutinize the prominent bulk properties of the resulting perovskites. In both spectra, a systematic bathochromic shift is conferred to Cs 0–20% in relation to the Cs amount, a piece of solid evidence for the Cs incorporation into the perovskite crystal lattices in line with precedent results [17]. Meanwhile, the shift for Cs 2.5% * is great nearly corresponding to that for Cs 15%. This sharply contrasts with the blue shift by Cs^+ in lead perovskites. Such discrepancy can arise from the size difference between Sn and Pb. On the other hand, the shift signifies the reduction of bandgap which was calculated by the absorption spectra to be 1.61, 1.60, 1.54, 1.49, 1.43, 1.36, and 1.44 eV for Cs 0–20% and 2.5%*, respectively. The addition of a small amount (2.5%) of Cs^+ led to a minimal change in bandgap perhaps resulting from localization at the exterior of perovskite crystals. However, more addition (5%) significantly reduces the bandgap. As referring to the literature, the bandgaps of tin perovskites are 1.40 eV for $FASnI_3$, 1.43 eV for $FASnI_3$ with 1% $EDAI_2$, and 1.50 eV for $GA_{0.2}FA_{0.8}SnI_3$ with 1% $EDAI_2$ [11,26], from which we can learn that even a small amount of $EDAI_2$ can markedly raise the bandgap. As compared to that of the last perovskite, Cs 2.5%* attains an appreciably small bandgap. This imparts that EDA^{2+} is extruded out of bulk while pushing Cs^+ to bulk by the fact that DMPU is non-selective to Cs (Figure S3). Taken together with the evidence from the photographs, the significant difference (by 0.16 eV) in bandgap between Cs 2.5% and 2.5%* crystallizes that a heterojunction

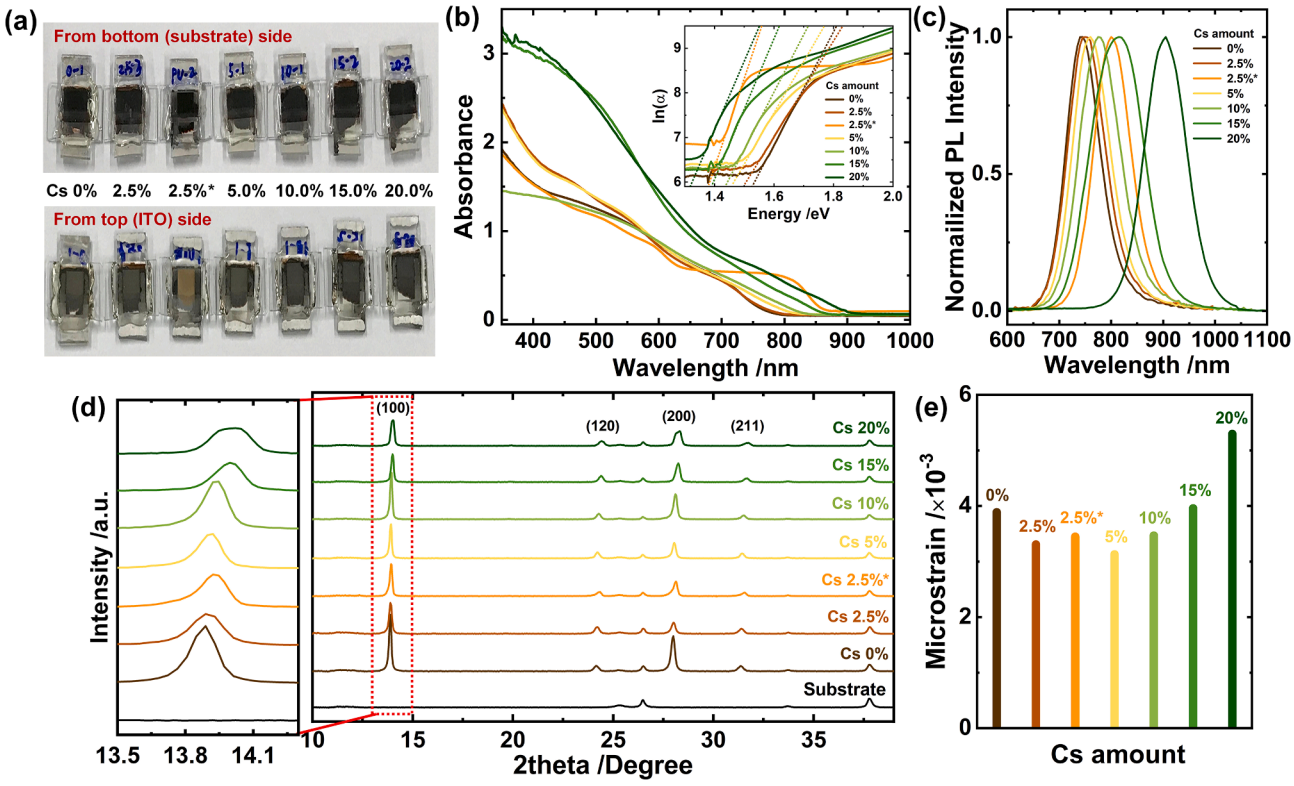

Fig. 3. (a) Photographs of the mesoporous TPSCs, encapsulated with soda-lime glasses, taken from the top and bottom sides. (b) Light absorption (inset: ln(α) versus energy (eV) where α stands for absorption coefficient) and (c) PL spectra, and (d) high-resolution XRD patterns and (e) microstrain of thin films of tin perovskites. The Cs 0–20% indicates $Cs_xGA_{0.2-x}FA_{0.8}SnI_3$ (x = 0–0.2) crystallized from the DMSO/DMF solvent while the Cs 2.5%* means $Cs_{0.025}GA_{0.175}FA_{0.8}SnI_3$ crystallized from the DMPU/DMF solvent.

is created for Cs 2.5%* where 3D hollow perovskite (with a large bandgap) is formed in the surface (near ITO) while a large body of 3D perovskite (with a small bandgap) is formed in bulk (in TiO_2/Al_2O_3). We note that EDA^{2+} passivates the exterior of the bulk 3D perovskite while resulting in heterojunction formation, which is distinct from others where the top surface of perovskites is mostly tailored. We depict the heterojunction in Figure S6c. On the other hand, this result is promising for future research regarding how to make the most use of a large proportion (>10%) of diammonium cations without the expense of bandgap. We speculate that in mesoscopic TPSCs crystal growth begins from the bottom where annealing evaporates solvents by breaking the solvents-SnI_2 complex for nucleation and crystallization. For the first 1 min DMF is vaporized to form 3D perovskite in bulk during which the EDA^{2+} is preferentially dissolved in DMPU. For the next 4 min, DMPU is vaporized to form 3D hollow perovskite in the surface with concentrating EDA^{2+} at the exterior of the 3D perovskite. In many cases, whereas a heterojunction is created by two deposition steps in other types of PSCs, the steps can be streamlined by the appropriate choice of cosolvents as we show in this work. Meanwhile, Urbach energy, a parameter to evaluate the quality of perovskite crystals, is calculated by slopes as seen in an inset of Fig. 3b. While 66.3–89.1 meV is given to Cs 0–20%, Cs 2.5%* attains the lowest energy of 48.3 meV (i.e., the sharpest slope). This imparts the least defective films by combined effects of Cs^+ and EDA^{2+} despite the heterojunction formation, and meanwhile, is lower than that for the spin-coated tin perovskites [41,57].

X-ray diffraction (XRD) analysis can corroborate and complement the results of optical properties. High-resolution XRD patterns are thus attained from the perovskites and presented in Fig. 3d. Overall, XRD peaks do not emerge on non-perovskite phases and continually shift on elevating the Cs amount to higher angles, in consistent with light absorption spectra. This is a result of the lattice shrinkage by contraction of the tin iodide octahedron because Cs^+ has a strong covalent and ionic interaction with iodide. This reduces the free energy and hence strengthens lattice stability. However, Cs 2.5% outputs Cs^+ which is populated at the exterior of perovskite crystals, as manifested by little displacement from Cs 0% in XRD peaks as well as revealed in light absorption spectra. This is desirable for surface passivation due to the strong interaction of Cs^+ and is in line with the optical properties. Incorporating Cs by as large as either ~15 or 20% adds an extra peak at a large angle noticeably in (1 0 0) and (2 0 0) crystal planes. We infer from the literature that excess Cs can incur phase separation [17]. As explicitly displayed in the peaks of the (1 0 0) plane, Cs 2.5%* shifts greater than Cs 2.5% and even than Cs 5% implying that lattice contraction is promoted not only by the Cs incorporation but also by the absence of large cations of EDA^{2+} in bulk. Replacing of bulky GA^+ with Cs^+ as much as 2.5% can make the Goldschmidt tolerance factor closest to 1, desirable for the ideal cubic structure of 3D perovskite (Table S8). As presented in Figure S8 and Table S9, the XRD patterns were digitized as lattice parameters by simulation using the TOPAS software. In spite of this, the 3D crystal structures are well preserved as judged by the presence of all signature peaks. On the other hand, the contraction did not involve the increasing bandgap that occurs by cesium in lead perovskites [58]. Instead, the contraction goes concurrent with relaxing lattice strain (except Cs 15% and 20%), Fig. 3e, for which the Williamson-Hall plots (Figure S9) were used. For example, Cs 2.5%* undergoes 11.3% reduction of lattice strain during 2.1% lattice contraction likely towards enhancing the geometric symmetry of the perovskite structure [17]. Illustrations shown in Fig. 2 briefly summarize the major behaviors of cations in this work.

Keeping the desirable film properties in mind, we now take a closer look at device properties. According to the earlier *J-V* results of the thick TPSCs (Fig. S2a and Table S3), the inclusion of >2.5% Cs does not elevate power conversion efficiency (PCE). At a large Cs content (≥5%) the solution infiltration proceeded slowly to a noticeable extent. The Cs inclusion might increase surface tension due to the strong ionic bond. To the end, the part of the TiO_2 scaffold in close proximity to the substrate remains vacant as visualized by cross-sectional scanning electron microscope (SEM) imaging shown in Figure S10. In striking contrast, the excellent infiltration of tin perovskites of Cs 0%, 2.5%, and 2.5%* was obtained. We need to remind that the limited infiltration can provoke degradation issues of device performance such for example as an attenuating collection of light and charge carriers, increasing defect density, and/or entrapping undesirable ingressive materials. Therefore, this can cancel the fair correlation of properties between films and devices. For this reason, we hereafter pay attention to the device properties

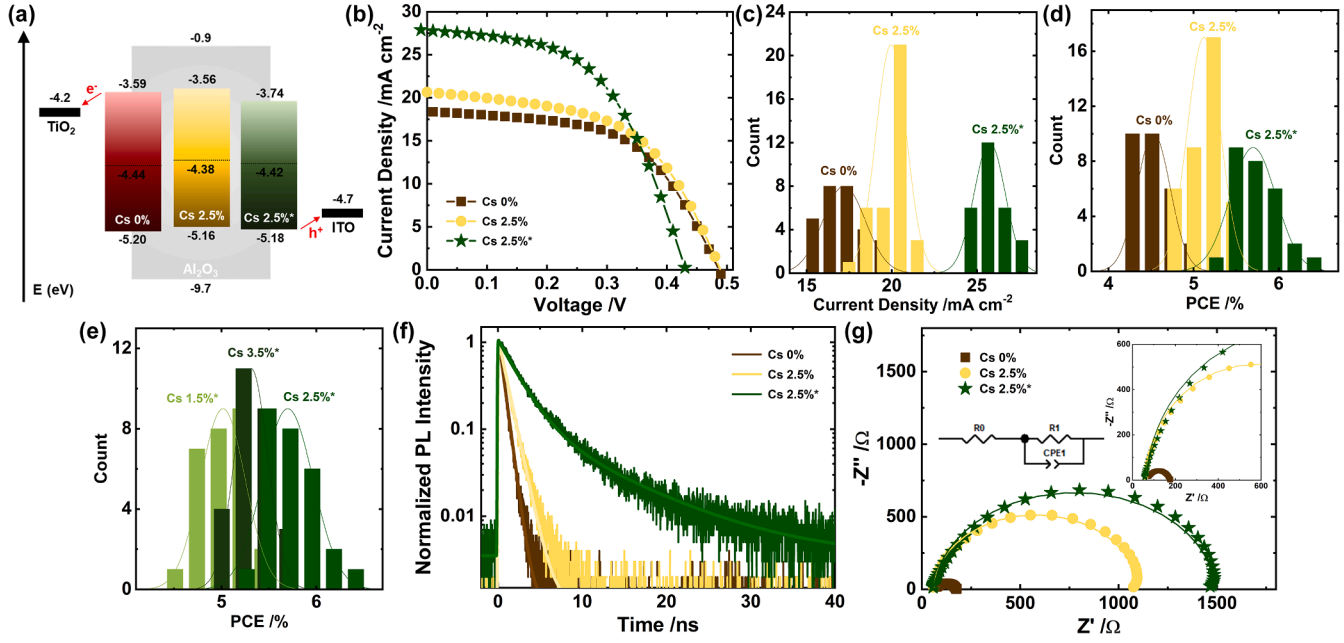

Fig. 4. (a) Energy diagram, (b) characteristic *J-V* curves, (c) J_{SC} and (d) PCE histograms (≥27 devices), (g) impedance spectra (insets: an equivalent circuit and a magnified figure) of TPSCs based on Cs 0%, 2.5%, and 2.5%*. (e) PCE histogram of TPSCs based on Cs 1.5%*, 2.5%*, and 3.5%* where the Cs 2.5%* is the same as in (d). (f) TCSPC spectra were obtained with the spin-coated films for reproducible and high-quality responses.

of Cs 0%, 2.5%, and 2.5%*. Fig. 4a sketches an energy diagram of the mesoporous thick TPSCs, constructed by the light absorption and ultraviolet photoelectron spectroscopy (UPS) whose data are exhibited in Figure S11. In accordance with the literature [3,10], the tin perovskites are shallow in energy levels of the conduction band minimum (CBM) and valence band maximum (VBM) as compared with lead counterparts. Cesium incorporation (Cs 0% → 2.5%) triggers an upward shift of CBM and VBM to a slight extent (0.03–0.04 eV) due to the lattice contraction for enhanced hybridization of tin and iodide orbitals. Heterojunction formation (Cs 2.5% → 2.5%*) greatly enhances the hybridization as well by repairing tin-iodide hollows. While narrowing the bandgap, it seemingly shifts both CBM and VBM downwardly. Structural variations perhaps associated with the microstrain besides hybridization strength might account for this [59]. Despite this, Cs 2.5%* is well paired especially with TiO_2, attaining reduced band offset for minimal open-circuit voltage (V_{OC}) deficit. Meanwhile, the relative uplifted Fermi level represents the least p-type behavior of Cs 2.5%, one reason for which would be associated with the density of Sn^{4+} defects discussed in the following section.

Fig. 4b exhibits representative *J-V* curves evaluated under standard one sun illumination conditions, from which PCEs were calculated to be 5.0, 5.4, and 6.4% for the Cs 0%, Cs 2.5%, and Cs 2.5%*, respectively. This is a ~20 percent rise from that previously marked for the large bandgap mesoscopic TPSCs [49]. Thanks to the semitransparency of ITO mesoporous PSCs [49], 1.5% of PCE can be augmented as near-infrared SCs were mechanically stacked on the bottom, Figure S12. The evolution of PCE is predominantly determined by rising J_{SC} (18.4, 20.7, and 27.8 mA cm^{-2}). Overall, the attained J_{SC} values are greater than that of the carbon-based TPSCs owing to the efficient light reflection of our ITO electrode [49]. Noteworthily, the J_{SC} leap from the Cs 2.5% to Cs 2.5%* is dramatic thanks to the significant shrinkage of bandgap which broadens the light-harvesting range over the cross-section of thick films of tin perovskites. Especially, the J_{SC} of Cs 2.5%* matches well with that calculated from IPCE spectra (Fig. 1b). These results are highly reproducible and histograms formulated from ≥27 devices are presented in Fig. 4c,d and Table S10–S12. Meanwhile, we have further attempted to enhance the device performance of Cs 2.5%* by incrementing annealing temperature, due to the high boiling point of DMPU, with a 10 °C rise from 100 °C to 120 °C or finely tuning the Cs amount by ±1%. The results of the former presented in Figure S13 and Table S13 confirm that there exist minimal variations, further confirmed by Cs 2.5%, and 100 °C is recommended from viewpoints of energy consumption. The results of the latter of PCE histogram (Fig. 4e) obtained from 27 devices present that the TPSC performance is susceptible to the Cs amount in a narrow range of 1.5–3.5% resembling lead-based analogue [60] and is augmented by neither Cs 1.5%* nor 3.5%* due to decreased V_{OC} and fill factor. All raw data of photovoltaic parameters are inserted in Table S14, S15. Whereas 1.5% is not sufficient to make Cs^+ intake effect, 3.5% might be excess to enhance defective states as evidenced in what follows. A similar amount of Cs^+ was used in our recent research [57]. On the other hand, the principal focus in this work is on cation and solvent engineering for 3D tin perovskites. Future work would proceed with improving their contact interfaces with TiO_2 and Al_2O_3 to elevate V_{OC} and FF.

The origin of photovoltaic performance is examined through measurements of time-correlated single-photon counting (TCSPC) and electrochemical impedance spectroscopy (EIS) techniques, as shown in Fig. 4f and g, respectively. Fig. 4f shows PL decay profiles of the thin films measured through TCSPC. The corresponding fitted decay coefficients are summarized in Table S16. In the profiles, the fast decay component is intimately associated with the non-radiative recombination of charge carriers via surface traps, and the slow decay component is linked to radiative recombination in bulk films. While Cs 0% and Cs 2.5% lack the slow decay components, the Cs incorporation led to that an average lifetime is extended from 0.59 to 0.95 ns. The recorded timescale is found similar to that for 3D hollow tin perovskites in literature [39]. As Cs^+ is populated for Cs 2.5%, the extended lifetime likely corroborates the Cs effect of surface passivation. We posit that the Sn-I bond is weak due to the shallow energy of Sn 5s orbital [22]. We thus speculate that by leveraging the strong bond Cs^+ might be able to hold dangling iodides in place. Both the fast and slow components were present for Cs 2.5%*. Each lifetime is 2.19 and 8.76 ns so that the average lifetime goes to 4.51 ns. Relative to Cs 2.5%, the 2.3-fold enhanced lifetime of the fast decay component represents the excellent surface passivation is endowed with Cs 2.5%*. We attribute this to surface passivation by EDA^{2+} at the exterior of perovskite crystals. Importantly, the presence of the slow component can result from the repairment of tin-iodide vacancies for suppressed recombination in bulk. It is worthy to note that the repairment would be beneficial for efficient charge transport as well. The TCSPC results impart that desirable bulk and surface properties, toward suppressing recombination, of tin perovskites are conferred to Cs 2.5%*.

Meanwhile, EIS is a powerful and non-destructive tool to investigate interfaces and shows great utility in many research areas including PSCs. EIS can complement the TCSPC results by offering insights into charge kinetics at a device level. Thus, the EIS measurements were carried out in dark at a frequency range of 1–10^6 Hz at open-circuit conditions. Nyquist plots exhibited in Fig. 4g show only single semicircles. This can be related to charge recombination at the perovskite interfaces (with ETM and/or HTM). The mesoporous TPSCs using not ITO but carbon electrodes often show two semicircles where the additional one appears at a high-frequency range for the relatively slow charge transfer at the contact interfaces [21]. The absence of the first semicircles in our plots underpins the favorable energetic alignments of the perovskites with ITO. By fitting the plots using an equivalent circuit model (shown in an inset of Fig. 4g), we acquired recombination resistances obeying the order Cs 2.5%* (1435 Ω) > Cs 2.5% (1033 Ω) > Cs 0% (107 Ω). The large resistance values represent high resistance to recombination. This is consistent with the TCSPC results. Taken together, the TCSPC and EIS results account for the enhanced passivation for charge collection and improved photovoltaic parameter – particularly J_{SC} – which is conferred to Cs 2.5%*. In most cases, the passivation should raise V_{OC}. However, this does not occur because of the significant bandgap shrinkage. Instead, a V_{OC} deficit is lowered to prove the efficient passivation.

Even though the experiments are performed in a nearly inert environment (i.e., glove box), the minute amounts of O_2 and H_2O are inevitable, which can accompany the oxidation of Sn (II). Fig. 5a-c of high-resolution XPS spectra show the proportion of Sn^{4+} (defects) to Sn^{2+}. Usually, the perovskite films in p-i-n TPSCs contain a large proportion of ≫10% Sn^{4+}. One reason may arise during spin-coating bringing constant ambient flow orthogonal to the substrate. Often, the similar proportions of Sn^{4+} defects are reported in p-i-n TPSCs. However, they use thin films (~200 nm) whereas we use thick films (~2 μm) of demanding quality. This flow can be more vigorous at a higher spin-rate (e.g., ≥5,000 rpm) which is commonly adopted for film uniformity of perovskites. In striking contrast, the small proportion of Sn^{4+} below 10% is attained by drop-casting. Importantly, the Cs 2.5%* attains the least Sn^{4+} of below 5% [33]. We postulate that such a small proportion of Sn^{4+} defects originates from significantly limited access of ingressive H_2O or O_2 through constraints of the mesopores and during the series of static experimental procedures for perovskite crystallization including drop-casting and annealing. Supporting illustrations of comparing spin-coating and drop-casting processes are shown in Figure S14. It is worthwhile noting that the absence or low proportion of Sn^{4+} is pivotal for stability as well as efficiency.

Ensuring longevity is weighty, lying ahead for practical use of tin perovskites and their applications. A great deal of relevant research on TPSCs has been performed where the reported time span is usually shorter than 1000 h irrespective of the differed test conditions [3,61,62]. We have herein adopted three test conditions for the mesoscopic TPSCs, including maximum power point tracking under continual standard one sun illumination with and without encapsulation (Fig. 5d) and dark

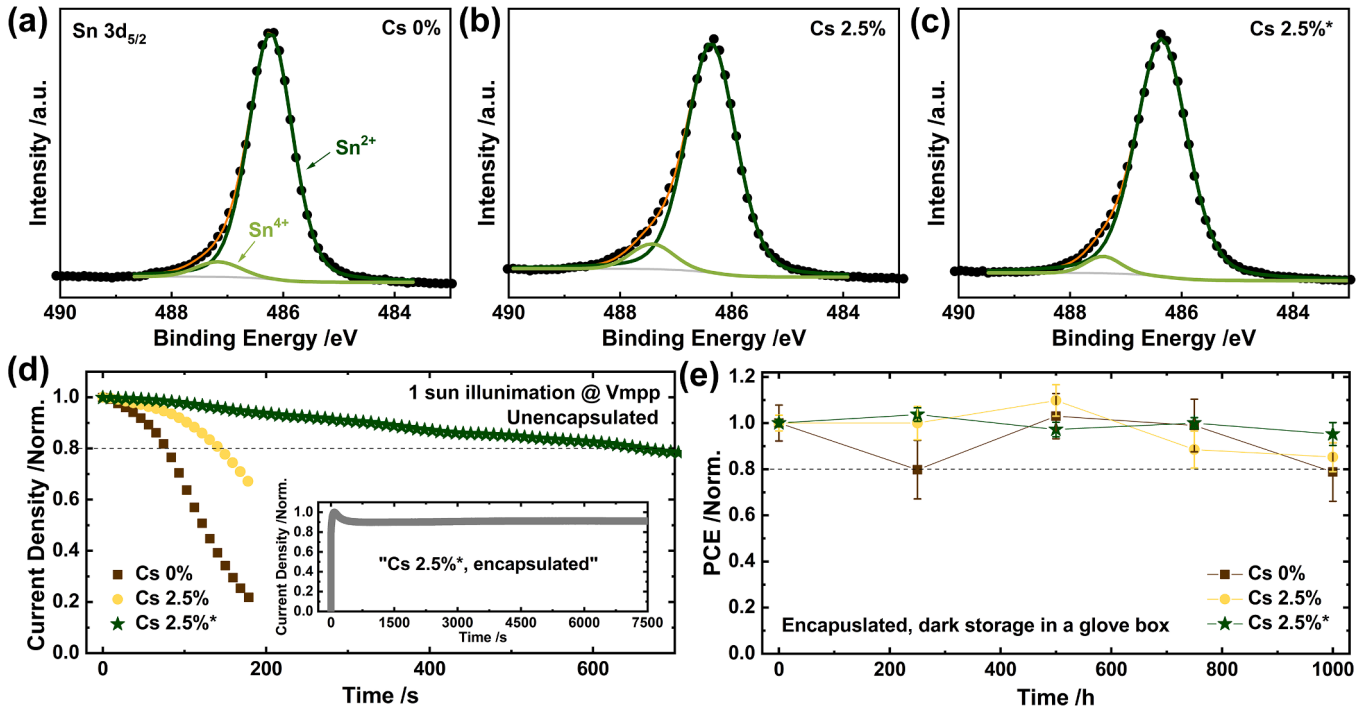

Fig. 5. (a-c) Sn 3d XPS spectra of thin films of the Cs 0%, 2.5%, and 2.5%* perovskites, where peaks of Sn^{2+} and Sn^{4+} are deconvoluted (proportions of Sn^{4+}: 5.5, 8.4, and 4.2%, respectively). Operational stability data of the mesoporous TPSCs plotted by (d) normalized current density and (e) PCE as a function of time. While 5 devices are used for each condition, (d) shows the representative data, and (e) shows the data points with standard deviation. They were measured (d) at maximum power points and under continual standard 1 sun light irradiation (inset: 7500 s tracking from an encapsulated device of Cs 2.5%*) and (e) intermittently during 1000 h dark storage in a glove box. Dotted lines are drawn for a guide for 80% of the initial value.

storage with encapsulation (Fig. 5e). All measurements were performed under ambient air. The incorporation of Cs extends life spans sizably. Taking one example, Cs 2.5% doubles the lifetime (~80 → ~145 s), i.e., retention time above 80% of the initial performance, without encapsulation (Fig. 5d). The extended life span stems from the stabilized lattice of perovskite crystals, besides the passivation, one benefit of which in device operation is excellent moisture- and photo-stability as validated in earlier efforts [17,60]. Meanwhile, the surface passivation by EDA^{2+} expands on the Cs^{+} effect. Its addition even at a small proportion (~1%) can be dramatic to device longevity towards the stabilized exterior of perovskite crystals, seamless contact between the crystals, and suppressed ion migration (particularly under bias voltage application) as already discovered in the literature [11,26]. In addition, in the heterojunction where the overlay of 3D hollow perovskite containing a large proportion of EDA^{2+} can play a role as an umbrella, high resistance to the aggressive ingression of O_2 and H_2O is added. Less amount (20 → 15%) of SnF_2, a well-known additive to suppress tin oxidation, was added to Cs 2.5%*. Nevertheless, Cs 2.5%* demonstrated a ~5-fold extended life span (~145 → ~660 s), relative to Cs 2.5%, for the 80% retention (Fig. 5d) without encapsulation. The excellent reproducibility of the results was attained, Figure S15. On the other hand, this is a ~10-fold extension from the old version of tin perovskites in the mesoscopic ITO PSCs [49].

It is identified that no encapsulation gives rise to short life spans under ambient measurements, in line with our earlier report [49]. However, this is not surprising if one takes into account that oxygen and water penetrating through the mesoporous scaffolds are abundant under ambient air. In particular, the oxygen abundance can incur formation of superoxide (O^{2-}) that is produced with ease in the presence of photo-excited electron and/or interstitial iodide, and is reactive to perovskite components such as organic cations [63]. Nevertheless, encapsulation substantially fixed this issue by allowing Cs 2.5%* to elongate the lifetime to 7500 s (the time for the 90% retention) at maximum power point tracking as an inset in Fig. 5d displays. This lifetime is competitive to p-i-n TPSCs [34,42]. Assuming thick films, along with heterojunction films in this work, can have high resistance to degradation, this result brings future prospects for practical applications. On the other hand, encapsulation rendered evaluation of stability over the time course of 1000 h, Fig. 5e, where devices are stored in a glove box and taken out for intermittent measurements. The 80% retention turned out to be a failure for Cs 0%, in contrast to others. Cs 2.5%* is least attenuated with merely a 5% drop whereas Cs 0% and 2.5% decline with 15 and 21% drops, respectively. What matters more is that Cs 2.5%* is least fluctuated due to the high stability even though the intermittent measurements exposing bias voltages and light can induce several pros and cons effects including photoreduction (enabling Sn^{4+} defect healing), ion migration, etc [29,30]. On the whole, our understanding of the stability landscape in mesoporous TPSCs will be momentous for future research efforts.

3. Conclusions

To fabricate a ~2 μm thick film of tin perovskite for broad intense light harvesting in triple mesoscopic PSCs, we have judiciously formulated a solution – $Cs_{0.025}GA_{0.175}FA_{0.8}SnI_3$ with 15% $EDAI_2$ and 15% SnF_2 – in a cosolvent of DMPU/DMF. Especially, the role of Cs cation is to enhance the performance and stability of perovskite crystals, exemplified by significantly reduced lattice strain during contraction, effective surface passivation, and moisture and photostability. Adopting DMPU suppresses tin defects (below 5%), protects crystal exterior, and prevents $EDAI_2$ from being embedded into bulk perovskite for efficient collection of light and charge carriers. The last results in formation of tin perovskite of 3D/hollow 3D heterojunction architecture. In the mesoscopic TPSCs, the resulting perovskite enables broad intense quantum efficiency exceeding 80% over a range of 400–780 nm (90.5% at 650 nm), and retaining >50% to 800 nm, which has not been achieved to the best of our knowledge by p-i-n TPSCs because of their thin film thickness (~200 nm). The high quantum efficiency leads to photocurrent as high as >27 mA cm^{-2}. Besides, the TPSCs are endowed with satisfactory

operational stability, manifested by merely a 5–10% drop at maximum power point light soaking for 6500 s and during 1000 h on shelf storage. The reported scheme herein is highly reproducible and merits further exploration of a myriad of cations and perovskites, and their energy and electronic applications including *n*-i-p PSCs.

Declaration of Competing Interest

The authors declare the following financial interests/personal relationships which may be considered as potential competing interests: Eric Wei-Guang Diau reports a relationship with National Science and Technology Council, Taiwan that includes: funding grants.

Data availability

Data will be made available on request.

Acknowledgments

This work is supported by the National Science and Technology Council (NSTC), Taiwan (Grant Nos. NSTC 111-2634-F-A49-007 and NSTC 111-2123-M-A49-001) and the Centre for Emergent Functional Matter Science of National Yang Ming Chiao Tung University (NYCU) from The Featured Areas Research Centre Program within the framework of the Higher Education Sprout Project by the Ministry of Education (MOE) in Taiwan.

Appendix A. Supplementary data

Supplementary data to this article can be found online at https://doi.org/10.1016/j.cej.2023.142635.

References

[1] H. Min, D.Y. Lee, J. Kim, G. Kim, K.S. Lee, J. Kim, M.J. Paik, Y.K. Kim, K.S. Kim, M. G. Kim, T.J. Shin, S. Il Seok, Perovskite solar cells with atomically coherent interlayers on SnO2 electrodes, Nature 598 (7881) (2021) 444–450.
[2] J. Jeong, M. Kim, J. Seo, H. Lu, P. Ahlawat, A. Mishra, Y. Yang, M.A. Hope, F. T. Eickemeyer, M. Kim, Y.J. Yoon, I.W. Choi, B.P. Darwich, S.J. Choi, Y. Jo, J. H. Lee, B. Walker, S.M. Zakeeruddin, L. Emsley, U. Rothlisberger, A. Hagfeldt, D. S. Kim, M. Grätzel, J.Y. Kim, Pseudo-halide anion engineering for α-FAPbI3 perovskite solar cells, Nature 592 (7854) (2021) 381–385.
[3] M. Konstantakou, T. Stergiopoulos, A critical review on tin halide perovskite solar cells, J. Mater. Chem. A 5 (23) (2017) 11518–11549.
[4] L. Lanzetta, J.M. Marin-Beloqui, I. Sanchez-Molina, D. Ding, S.A. Haque, Two-Dimensional Organic Tin Halide Perovskites with Tunable Visible Emission and Their Use in Light-Emitting Devices, ACS Energy Lett. 2 (7) (2017) 1662–1668.
[5] A. Waleed, M.M. Tavakoli, L. Gu, Z. Wang, D. Zhang, A. Manikandan, Q. Zhang, R. Zhang, Y.-L. Chueh, Z. Fan, Lead-Free Perovskite Nanowire Array Photodetectors with Drastically Improved Stability in Nanoengineering Templates, Nano Lett. 17 (1) (2017) 523–530.
[6] S. Shao, W. Talsma, M. Pitaro, J. Dong, S. Kahmann, A.J. Rommens, G. Portale, M. A. Loi, Field-Effect Transistors Based on Formamidinium Tin Triiodide Perovskite, Adv. Funct. Mater. 31 (2021) 2008478.
[7] G. Xing, M.H. Kumar, W.K. Chong, X. Liu, Y. Cai, H. Ding, M. Asta, M. Grätzel, S. Mhaisalkar, N. Mathews, T.C. Sum, Solution-Processed Tin-Based Perovskite for Near-Infrared Lasing, Adv. Mater. 28 (37) (2016) 8191–8196.
[8] P. Zhou, H. Chen, Y. Chao, Q. Zhang, W. Zhang, F. Lv, L. Gu, Q. Zhao, N. Wang, J. Wang, S. Guo, Single-atom Pt-I3 sites on all-inorganic Cs2SnI6 perovskite for efficient photocatalytic hydrogen production, Nat. Commun. 12 (2021) 4412.
[9] J. Cao, Z. Guo, S. Zhu, Y. Fu, H. Zhang, Q. Wang, Z. Gu, Preparation of Lead-free Two-Dimensional-Layered (C8H17NH3)2SnBr 4 Perovskite Scintillators and Their Application in X-ray Imaging, ACS Appl. Mater. Interfaces 12 (17) (2020) 19797–19804.
[10] N. Sun, W. Gao, H.e. Dong, Y. Liu, X. Liu, Z. Wu, L. Song, C. Ran, Y. Chen, Architecture of p-i-n Sn-Based Perovskite Solar Cells: Characteristics Advances, and Perspectives, ACS Energy Lett. 6 (8) (2021) 2863–2875.
[11] E. Jokar, C.-H. Chien, C.-M. Tsai, A. Fathi, E.-W.-G. Diau, Robust Tin-Based Perovskite Solar Cells with Hybrid Organic Cations to Attain Efficiency Approaching 10%, Adv. Mater. 31 (2019) 1804835.
[12] S. Shao, J. Liu, G. Portale, H.-H. Fang, G.R. Blake, G.H. ten Brink, L.J.A. Koster, M. A. Loi, Highly Reproducible Sn-Based Hybrid Perovskite Solar Cells with 9% Efficiency, Adv. Energy Mater. 8 (2018) 1702019.
[13] Z. Zhao, F. Gu, Y. Li, W. Sun, S. Ye, H. Rao, Z. Liu, Z. Bian, C. Huang, Mixed-Organic-Cation Tin Iodide for Lead-Free Perovskite Solar Cells with an Efficiency of 8.12%, Adv. Sci. 4 (2017) 1700204.
[14] K. Nishimura, M.A. Kamarudin, D. Hirotani, K. Hamada, Q. Shen, S. Iikubo, T. Minemoto, K. Yoshino, S. Hayase, Lead-free tin-halide perovskite solar cells with 13% efficiency, Nano Energy 74 (2020), 104858.
[15] Y. Liao, H. Liu, W. Zhou, D. Yang, Y. Shang, Z. Shi, B. Li, X. Jiang, L. Zhang, L. N. Quan, R. Quintero-Bermudez, B.R. Sutherland, Q. Mi, E.H. Sargent, Z. Ning, Highly Oriented Low-Dimensional Tin Halide Perovskites with Enhanced Stability and Photovoltaic Performance, J. Am. Chem. Soc. 139 (19) (2017) 6693–6699.
[16] M. Hu, R. Nie, H. Kim, J. Wu, S. Chen, B.-W. Park, G. Kim, H.-W. Kwon, S.I. Seok, Regulating the Surface Passivation and Residual Strain in Pure Tin Perovskite Films, ACS Energy Lett. 6 (10) (2021) 3555–3562.
[17] P. Pansa-Ngat, H. Nakajima, R. Supruangnet, S. Suwanna, P. Pakawatpanurut, S. Sahasithiwat, P. Kanjanaboos, Phase Evolution in Lead-Free Cs-Doped FASnI3 Hybrid Perovskites and Optical Properties, J. Phys. Chem. C 125 (31) (2021) 16903–16912.
[18] B.-B. Yu, Z. Chen, Y. Zhu, Y. Wang, B. Han, G. Chen, X. Zhang, Z. Du, Z. He, Heterogeneous 2D/3D Tin-Halides Perovskite Solar Cells with Certified Conversion Efficiency Breaking 14%, Adv. Mater. 33 (2021) 2102055.
[19] H. Li, X. Jiang, Q.i. Wei, Z. Zang, M. Ma, F. Wang, W. Zhou, Z. Ning, Low-Dimensional Inorganic Tin Perovskite Solar Cells Prepared by Templated Growth, Angew. Chem. Int. Ed. 60 (30) (2021) 16330–16336.
[20] K.P. Marshall, M. Walker, R.I. Walton, R.A. Hatton, Enhanced stability and efficiency in hole-transport-layer-free CsSnI3 perovskite photovoltaics, Nat. Energy 1 (2016) 16178.
[21] C.-M. Tsai, N. Mohanta, C.-Y. Wang, Y.-P. Lin, Y.-W. Yang, C.-L. Wang, C.-H. Hung, E.-G. Diau, Formation of Stable Tin Perovskites Co-crystallized with Three Halides for Carbon-Based Mesoscopic Lead-Free Perovskite Solar Cells, Angew. Chem. Int. Ed. 56 (44) (2017) 13819–13823.
[22] M. Rameez, E.-R. Lin, P. Raghunath, S. Narra, D. Song, M.-C. Lin, C.-H. Hung, E.-G. Diau, Development of Hybrid Pseudohalide Tin Perovskites for Highly Stable Carbon-Electrode Solar Cells, ACS Appl. Mater. Interfaces 12 (19) (2020) 21739–21747.
[23] C. Wang, F. Gu, Z. Zhao, H. Rao, Y. Qiu, Z. Cai, G. Zhan, X. Li, B. Sun, X. Yu, B. Zhao, Z. Liu, Z. Bian, C. Huang, Self-Repairing Tin-Based Perovskite Solar Cells with a Breakthrough Efficiency Over 11%, Adv. Mater. 32 (2020) 1907623.
[24] Q. Tai, X. Guo, G. Tang, P. You, T.-W. Ng, D. Shen, J. Cao, C.-K. Liu, N. Wang, Y. e. Zhu, C.-S. Lee, F. Yan, Antioxidant Grain Passivation for Air-Stable Tin-Based Perovskite Solar Cells, Angew. Chem. Int. Ed. 58 (3) (2019) 806–810.
[25] W. Liao, D. Zhao, Y. Yu, C.R. Grice, C. Wang, A.J. Cimaroli, P. Schulz, W. Meng, K. Zhu, R.-G. Xiong, Y. Yan, Lead-Free Inverted Planar Formamidinium Tin Triiodide Perovskite Solar Cells Achieving Power Conversion Efficiencies up to 6.22%, Adv. Mater. 28 (42) (2016) 9333–9340.
[26] E. Jokar, C.-H. Chien, A. Fathi, M. Rameez, Y.-H. Chang, E.-G. Diau, Slow surface passivation and crystal relaxation with additives to improve device performance and durability for tin-based perovskite solar cells, Energy Environ. Sci. 11 (9) (2018) 2353–2362.
[27] S.J. Lee, S.S. Shin, Y.C. Kim, D. Kim, T.K. Ahn, J.H. Noh, J. Seo, S.I. Seok, Fabrication of Efficient Formamidinium Tin Iodide Perovskite Solar Cells through SnF2–Pyrazine Complex, J. Am. Chem. Soc. 138 (12) (2016) 3974–3977.
[28] X. Liu, T. Wu, J.-Y. Chen, X. Meng, X. He, T. Noda, H. Chen, X. Yang, H. Segawa, Y. Wang, L. Han, Templated growth of FASnI3 crystals for efficient tin perovskite solar cells, Energy Environ. Sci. 13 (9) (2020) 2896–2902.
[29] E. Jokar, H.-S. Chuang, C.-H. Kuan, H.-P. Wu, C.-H. Hou, J.-J. Shyue, E. Wei-Guang Diau, Slow Passivation and Inverted Hysteresis for Hybrid Tin Perovskite Solar Cells Attaining 13.5% via Sequential Deposition, J. Phys. Chem. Lett. 12 (41) (2021) 10106–10111.
[30] J. Sanchez-Diaz, R.S. Sánchez, S. Masi, M. Krečmarová, A.O. Alvarez, E.M. Barea, J. Rodriguez-Romero, V.S. Chirvony, J.F. Sánchez-Royo, J.P. Martinez-Pastor, I. Mora-Seró, Tin perovskite solar cells with >1,300 h of operational stability in N2 through a synergistic chemical engineering approach, Joule 6 (2022) 861–883.
[31] M. Liu, H. Pasanen, H. Ali-Löytty, A. Hiltunen, K. Lahtonen, S. Qudsia, J.-H. Smått, M. Valden, N.V. Tkachenko, P. Vivo, B-Site Co-Alloying with Germanium Improves the Efficiency and Stability of All-Inorganic Tin-Based Perovskite Nanocrystal Solar Cells, Angew. Chem. Int. Ed. 59 (49) (2020) 22117–22125.
[32] X. Liu, K. Yan, D. Tan, X. Liang, H. Zhang, W. Huang, Solvent Engineering Improves Efficiency of Lead-Free Tin-Based Hybrid Perovskite Solar Cells beyond 9%, ACS Energy Lett. 3 (11) (2018) 2701–2707.
[33] D. Di Girolamo, J. Pascual, M.H. Aldamasy, Z. Iqbal, G. Li, E. Radicchi, M. Li, S.-H. Turren-Cruz, G. Nasti, A. Dallmann, F. De Angelis, A. Abate, Solvents for Processing Stable Tin Halide Perovskites, ACS Energy Lett. 6 (3) (2021) 959–968.
[34] E. Jokar, P.-Y. Cheng, C.-Y. Lin, S. Narra, S. Shahbazi, E. Wei-Guang Diau, Enhanced Performance and Stability of 3D/2D Tin Perovskite Solar Cells Fabricated with a Sequential Solution Deposition, ACS Energy Lett. 6 (2) (2021) 485–492.
[35] X. Liu, Y. Wang, T. Wu, X. He, X. Meng, J. Barbaud, H. Chen, H. Segawa, X. Yang, L. Han, Efficient and stable tin perovskite solar cells enabled by amorphous-polycrystalline structure, Nat. Commun. 11 (2020) 2678.
[36] G. Li, Z. Su, M. Li, F. Yang, M.H. Aldamasy, J. Pascual, F. Yang, H. Liu, W. Zuo, D. Di Girolamo, Z. Iqbal, G. Nasti, A. Dallmann, X. Gao, Z. Wang, M. Saliba, A. Abate, Ionic Liquid Stabilizing High-Efficiency Tin Halide Perovskite Solar Cells, Adv. Energy Mater. 11 (2021) 2101539.
[37] X. Jiang, H. Li, Q. Zhou, Q.i. Wei, M. Wei, L. Jiang, Z. Wang, Z. Peng, F. Wang, Z. Zang, K. Xu, Y.i. Hou, S. Teale, W. Zhou, R. Si, X. Gao, E.H. Sargent, Z. Ning, One-Step Synthesis of SnI2·(DMSO)x Adducts for High-Performance Tin Perovskite Solar Cells, J. Am. Chem. Soc. 143 (29) (2021) 10970–10976.

[38] X. Meng, Y. Wang, J. Lin, X. Liu, X. He, J. Barbaud, T. Wu, T. Noda, X. Yang, L. Han, Surface-Controlled Oriented Growth of FASnI3 Crystals for Efficient Lead-free Perovskite Solar Cells, Joule 4 (4) (2020) 902–912.
[39] W. Ke, C.C. Stoumpos, M. Zhu, L. Mao, I. Spanopoulos, J. Liu, O.Y. Kontsevoi, M. Chen, D. Sarma, Y. Zhang, M.R. Wasielewski, M.G. Kanatzidis, Enhanced photovoltaic performance and stability with a new type of hollow 3D perovskite {en}FASnI3, Sci. Adv. 3 (2022) e1701293.
[40] B.o. Li, B. Chang, L.u. Pan, Z. Li, L. Fu, Z. He, L. Yin, Tin-Based Defects and Passivation Strategies in Tin-Related Perovskite Solar Cells, ACS Energy Lett. 5 (12) (2020) 3752–3772.
[41] X. Jiang, F. Wang, Q. Wei, H. Li, Y. Shang, W. Zhou, C. Wang, P. Cheng, Q. Chen, L. Chen, Z. Ning, Ultra-high open-circuit voltage of tin perovskite solar cells via an electron transporting layer design, Nat. Commun. 11 (2020) 1245.
[42] D. Song, S. Narra, M.-Y. Li, J.-S. Lin, E.-G. Diau, Interfacial Engineering with a Hole-Selective Self-Assembled Monolayer for Tin Perovskite Solar Cells via a Two-Step Fabrication, ACS Energy Lett. 6 (12) (2021) 4179–4186.
[43] Z. Zhu, C.-C. Chueh, N. Li, C. Mao, A.-K.-Y. Jen, Realizing Efficient Lead-Free Formamidinium Tin Triiodide Perovskite Solar Cells via a Sequential Deposition Route, Adv. Mater. 30 (2018) 1703800.
[44] S. Shahbazi, M.-Y. Li, A. Fathi, E.-G. Diau, Realizing a Cosolvent System for Stable Tin-Based Perovskite Solar Cells Using a Two-Step Deposition Approach, ACS Energy Lett. 5 (8) (2020) 2508–2511.
[45] Z. Chen, B. Turedi, A.Y. Alsalloum, C. Yang, X. Zheng, I. Gereige, A. AlSaggaf, O. F. Mohammed, O.M. Bakr, Single-Crystal MAPbI3 Perovskite Solar Cells Exceeding 21% Power Conversion Efficiency, ACS Energy Lett. 4 (6) (2019) 1258–1259.
[46] E.L. Lim, A. Hagfeldt, D. Bi, Toward highly efficient and stable Sn2+ and mixed Pb2+/Sn2+ based halide perovskite solar cells through device engineering, Energy Environ. Sci. 14 (6) (2021) 3256–3300.
[47] B. Wu, Y. Zhou, G. Xing, Q. Xu, H.F. Garces, A. Solanki, T.W. Goh, N.P. Padture, T. C. Sum, Long Minority-Carrier Diffusion Length and Low Surface-Recombination Velocity in Inorganic Lead-Free CsSnI3 Perovskite Crystal for Solar Cells, Adv. Funct. Mater. 27 (2017) 1604818.
[48] F. Hao, C.C. Stoumpos, P. Guo, N. Zhou, T.J. Marks, R.P.H. Chang, M.G. Kanatzidis, Solvent-Mediated Crystallization of CH3NH3SnI3 Films for Heterojunction Depleted Perovskite Solar Cells, J. Am. Chem. Soc. 137 (35) (2015) 11445–11452.
[49] D. Song, L.Y. Hsu, C.-M. Tseng, E.-G. Diau, Solution-processed ITO nanoparticles as hole-selective electrodes for mesoscopic lead-free perovskite solar cells, Mater. Adv. 2 (2) (2021) 754–759.
[50] H. Ban, T. Zhang, X. Gong, Q. Sun, X.-L. Zhang, N. Pootrakulchote, Y. Shen, M. Wang, Fully Inorganic CsSnI3 Mesoporous Perovskite Solar Cells with High Efficiency and Stability via Coadditive Engineering, Sol. RRL 5 (2021) 2100069.
[51] T. Wu, X. Liu, X. Luo, H. Segawa, G. Tong, Y. Zhang, L.K. Ono, Y. Qi, L. Han, Heterogeneous FASnI3 Absorber with Enhanced Electric Field for High-Performance Lead-Free Perovskite Solar Cells, Nano-Micro Lett. 14 (2022) 99.
[52] S. Shao, J. Dong, H. Duim, G.H. ten Brink, G.R. Blake, G. Portale, M.A. Loi, Enhancing the crystallinity and perfecting the orientation of formamidinium tin iodide for highly efficient Sn-based perovskite solar cells, Nano Energy 60 (2019) 810–816.
[53] K. Chen, P. Wu, W. Yang, R. Su, D. Luo, X. Yang, Y. Tu, R. Zhu, Q. Gong, Low-dimensional perovskite interlayer for highly efficient lead-free formamidinium tin iodide perovskite solar cells, Nano Energy 49 (2018) 411–418.
[54] K. Park, J.-H. Lee, J.-W. Lee, Surface Defect Engineering of Metal Halide Perovskites for Photovoltaic Applications, ACS Energy Lett. 7 (3) (2022) 1230–1239.
[55] A.J. Doolin, R.G. Charles, C.S.P. De Castro, R.G. Rodriguez, E.V. Péan, R. Patidar, T. Dunlop, C. Charbonneau, T. Watson, M.L. Davies, Sustainable solvent selection for the manufacture of methylammonium lead triiodide (MAPbI3) perovskite solar cells, Green Chem. 23 (6) (2021) 2471–2486.
[56] J. Dong, S. Shao, S. Kahmann, A.J. Rommens, D. Hermida-Merino, G.H. ten Brink, M.A. Loi, G. Portale, Mechanism of Crystal Formation in Ruddlesden-Popper Sn-Based Perovskites, Adv. Funct. Mater. 30 (2020) 2001294.
[57] C.-H. Kuan, J.-M. Chih, Y.-C. Chen, B.-H. Liu, C.-H. Wang, C.-H. Hou, J.-J. Shyue, E. w.-g., Diau, Additive Engineering with Triple Cations and Bifunctional Sulfamic Acid for Tin Perovskite Solar Cells Attaining a PCE Value of 12.5% without Hysteresis, ACS Energy Lett. 7 (2022) 4436–4442.
[58] R. Prasanna, A. Gold-Parker, T. Leijtens, B. Conings, A. Babayigit, H.-G. Boyen, M. F. Toney, M.D. McGehee, Band Gap Tuning via Lattice Contraction and Octahedral Tilting in Perovskite Materials for Photovoltaics, J. Am. Chem. Soc. 139 (32) (2017) 11117–11124.
[59] S. Tao, I. Schmidt, G. Brocks, J. Jiang, I. Tranca, K. Meerholz, S. Olthof, Absolute energy level positions in tin- and lead-based halide perovskites, Nat. Commun. 10 (2019) 2560.
[60] G. Kim, H. Min, K.S. Lee, D.Y. Lee, S.M. Yoon, S.I. Seok, Impact of strain relaxation on performance of α-formamidinium lead iodide perovskite solar cells, Science 370 (6512) (2020) 108–112.
[61] A. Abate, Perovskite Solar Cells Go Lead Free, Joule 1 (4) (2017) 659–664.
[62] M. Pitaro, E.K. Tekelenburg, S. Shao, M.A. Loi, Tin Halide Perovskites: From Fundamental Properties to Solar Cells, Adv. Mater. 34 (2022) 2105844.
[63] N. Aristidou, C. Eames, I. Sanchez-Molina, X. Bu, J. Kosco, M.S. Islam, S.A. Haque, Fast oxygen diffusion and iodide defects mediate oxygen-induced degradation of perovskite solar cells, Nat. Commun. 8 (2017) 15218.